Opto-Electronics Review

journal homepage: https://journals.pan.pl/opelre

Source data encoding and beam generation in underwater optical communication using Laguerre-Gaussian modes

Aravind JM[1*], Arul Teen YP[2]

[1] Department of Electronics and Communication Engineering, Mar Ephraem College of Engineering and Technology, Marthandam, Tamil Nadu 629171, India
[2] Department of Electronics and Communication Engineering, University College of Engineering, Nagercoil, Tamil Nadu 629004, India

Article info

Article history:
Received 20 Feb 2025
Received in revised form 07 May 2025
Accepted 07 May 2025
Available on-line 11 Aug. 2025

Keywords:
underwater wireless optical communication;
Laguerre-Gaussian modes;
Res-GoogleNet;
Bessel-Gaussian beam;
spatial light modulator.

Abstract

Underwater wireless optical communication (UWOC) is a promising solution for high-speed data transfer in marine environments. However, underwater turbulence and scattering significantly degrade signal integrity. The objective of this study is to enhance the reliability and efficiency of underwater communication systems by improving signal decoding accuracy in the presence of distortion. In this paper, a novel approach to source data encoding and beam generation in underwater optical communication using Laguerre-Gaussian (LG) modes is proposed. Initially, the conversion of source data into digital code is followed by mode matching, which encodes data into specific phase modes. A Bessel-Gaussian laser beam is generated to carry the encoded information, which is then transformed into LG beams using a spatial light modulator (SLM). These beams, characterised by their orbital angular momentum (OAM) properties, propagate through various underwater environments, including pure seawater, coastal seawater, and turbid water, which introduce different levels of distortion. Distorted LG beams are captured by an underwater camera and processed by a computer. A deep learning model, Res-GoogleNet, is employed to accurately recognize the mode and decode the distorted OAM patterns. Finally, the decoded mode information is used to reconstruct the original data, ensuring efficient and reliable underwater communication. The efficacy of the proposed technique is assessed using Matlab-2019b, the underwater optical communication system is discovered on a Windows OS using 16 GB of RAM and an Intel Core i7 CPU. The proposed model improves accuracy, evaluation metrics of accuracy, precision, recall, signal-to-noise ratio (SNR) and bit error rate (BER). The proposed model achieves a high accuracy rate of 99.07%, surpassing the efficiency of existing approaches. The proposed model improves its accuracy by 5.47%, 1.80%, 0.62%, and 2.97% compared to a diffractive deep neural network (DDNN), a multichannel neural network (MCNN), and a deep convolutional neural network radio frequency (DCNN-RF), respectively.

1. Introduction

Underwater wireless optical communication (UWOC) has recently gained popularity due to its potential applications in high-speed wireless transmission and wide optical bands [1]. While UWOC technologies employ acoustic waves to communicate information with limited bandwidth (kHz) and large transmission latencies, they can dramatically enhance possible data speeds of up to Gbps while maintaining a low transmission latency [2].

However, while propagating in UWOC channels, optical beams experience turbulence, scattering, and absorption effects [3]. When photons interact with water molecules and other particles, they cause them to thermally lose energy, a phenomenon known as the irreversible absorption effect. Each photon broadcast direction varies randomly during the scattering event, which lowers the amount of energy that the receiver can absorb [4, 5]. Furthermore,

*Corresponding author at: jamesaravind@gmail.com

https://doi.org/10.24425/opelre.2025.154749
1896-3757/ Association of Polish Electrical Engineers (SEP) and Polish Academic of Sciences (PAS). Published by PAS

random changes in the undersea medium, primarily caused by differences in temperature and salinity, lead to optical turbulence [6]. These propagation effects have non-neglectable implications on signal detection (SD) as they make it difficult to get precise channel estimations.

UWOC has sparked significant attention in academic and business community as a viable solution to meet the constantly expanding demands of underwater high-data-rate transmission. UWOC systems outperform traditional, commonly used acoustic communication methods in terms of bandwidth, latency, and security [7]. Because of its significant intrinsic qualities, it is a prospective alternative or complementary for a wide range of underwater applications, including photography for natural ocean resource research [8]. Furthermore, future sixth-generation (6G) coverage is expected to extend to rural areas, water surfaces, underwater, and satellite scenarios, resulting in an integrated communication network that connects air, space, ground, and sea [9]. Due to its extensive frequency spectrum bandwidth resources, it is also considered one of the most promising technologies for 6G underwater high-capacity wireless communication scenarios [10].

Underwater acoustic communication (UAC) technology is the mainstay of traditional underwater communication [11]. It has been investigated for data transmission over long distances, up to several tens of kilometres, by utilising the low attenuation property made possible by the physical characteristics of sound waves propagating in water [12]. However, due to its narrow modulation bandwidth (only tens of kHz), UAC has a low-data-rate constraint [13]. Due to the poor acoustic wave propagation speed in the underwater channel, there is a lag of around 0.67 s/km [14]. Underwater radio frequency (RF) communication has a higher attenuation coefficient than UAC owing to the poor conductivity of electromagnetic waves in water, resulting in a significantly shorter transmission distance [15]. To overcome these issues, a novel approach to encoding source data and generating beams in underwater optical communication using Laguerre-Gaussian (LG) modes has been proposed. The significant contribution of the work has been as follows:

- The primary objective of the proposed underwater optical communication system is to leverage structured light beams (LG) for enhanced signal robustness in different water conditions.
- Developing the use of LG beams for mode-division multiplexing (MDM) in underwater communication.
- Deep learning-based mode recognition using Res-GoogleNet for accurate classification and decoding received optical modes, mitigating underwater turbulence effects.
- Using a spatial light modulator (SLM) to modulate Bessel-Gaussian beams into structured LG modes for improved underwater transmission.
- Evaluating the effectiveness of this method, several metrics are used including accuracy, precision, F1 score, recall, bit error rate (BER), and signal-to-noise ratio (SNR).

The remaining sections of the work are as follows: section 2 presents the literature review, section 3 outlines the proposed methodology, section 4 presents the results and discussion, and section 5 concludes the proposed work.

2. Literature review

In 2021, Wang *et al*. [16] proposed a unified model utilising a photon tracing approach for system performance analysis and underwater channel characterisation in the presence of solar noise. According to simulation data, the multiple scattering phenomena are closely related to multipath dispersion. When paired with a wide aperture, a restricted field of vision (FOV) allows the system to function at its best while also reducing the effects of ambient noise and delay spread.

In 2022, Zhan *et al*. [17] recommended an adaptive optics (AO) system based on a diffractive deep neural network (DDNN) to compensate for the distortion caused by optical turbulence (OT). According to the experimental findings, the suggested technique can rapidly extract the distorted vortex beam intensity pattern features, and the anticipated compensation phase screen can promptly correct the distortion caused by OT.

In 2024, Li *et al*. [18] proposed a deep convolutional neural network-RF (DCNN-RF) mode recognition model that extracts the red-green-blue (RGB) and hue-saturation-value (HSV) multidimensional feature information of the orbital angular momentum (OAM) mode picture using a dual-channel convolutional neural network (CNN). After merging Adam optimizer settings to optimize the CNN model, the OAM mode is identified by fusing the retrieved multidimensional features using an RF classifier.

In 2024, Wang *et al*. [19] suggested creating the best beams for propagation across air turbulence using a deep learning approach. To enable self-supervised learning and eliminate the need for pre-calculated datasets, an end-to-end implementation framework is created. Wave optics models and testing verify the synthesised beam effectiveness.

In 2024, Bai *et al*. [20] suggested a multichannel neural network (MCNN) that uses multi-feature fusion, data augmentation, and multichannel feature extraction to aid in the categorization of maritime synthetic aperture radars (SAR) scenes for limited oceanic data sets. The authors' MCNN framework has demonstrated exceptional classification capabilities through a thorough experimental investigation, achieving an average F-score of 95%, an average accuracy rate of 96%, and an average recall rate of 95% across 10 different maritime phenomena. Remarkably, it outperforms two state-of-the-art classification techniques, CMwv and AlexNet, by 18.3% and 23.7%, respectively.

In 2024, Peng *et al*. [21] suggested a vector vortex beam (VVB) classification approach to identify VVBs with polarization states that change continuously under atmospheric turbulence (AT). The experimental findings and numerical simulations demonstrate the accuracy of the suggested method in classifying tasks. The classification accuracy remains above 95% for different turbulence strengths, while the energy distribution percentage remains above 95% from weak to medium AT.

In 2024, Yang *et al*. [22] proposed a unique time-frequency synchronization method for the orthogonal frequency division multiplexing (OFDM) communication model. Through simulations and pool and lake investigations, the effectiveness and robustness of the developed model have been validated. The simulation experiment shows that, compared to the prior method, the proposed

strategy significantly enhances timing accuracy and CFO estimation accuracy and has a wider CFO detection range.

In 2024, Mohamed *et al*. [23] presented a brand-new image cryptosystem intended to increase UWOC systems security and dependability, especially for water bodies with greater scattering and absorption coefficients.

In 2024, Xing *et al*. [24] proposed a polar code-based embedded side information (SI) transmission technique that reduces peak-to-average power ratio (PAPR) using the partial transmit sequence (PTS) model for an underwater acoustic (UWA) OFDM communication model. The suggested integrated SI transmission strategy may significantly reduce the overall symbol error caused by SI faults, according to simulation and tank experiment results.

In 2024, Alraie *et al*. [25] suggested the OFDM subcarrier power modulation (SPM) system is intended to enhance the UWA data-rate communication system. The OFDM transmitting system gains the second dimension in the UWA communication system thanks to OFDM SPM. This contributes to the OFDM system data rate being doubled by doubling the transmission-side data stream. To examine throughput and BER, an equalizer was employed.

3. Proposed methodology

In this section, a novel source data encoding and beam generation in UWOC using LG modes have been proposed. Initially, the conversion of source data into a digital code is proposed, followed by mode matching to encode the data into specific phase modes. A Bessel-Gaussian laser beam is generated to carry the encoded information, which is then transformed into LG beams using an SLM. These beams, characterised by their OAM properties, propagate through various underwater environments, including pure seawater, coastal seawater, and turbid water, which introduce different levels of distortion. The use of LG beams with OAM in this work is motivated by their ability to maintain structural integrity in turbulent underwater environments. OAM beams exhibit a self-reconstructing property due to the angular momentum conservation, enabling them to resist distortion caused by scattering. While elliptically polarized beams also show similar structure-preserving effects [26], OAM beams offer a significant advantage by supporting multiple orthogonal modes, making them ideal for MDM. The distorted LG beams are captured by an underwater camera and processed by a computer. A DL model, Res-GoogleNet, is employed to accurately recognize the mode and decode the distorted OAM patterns. Finally, the decoded mode information is used to reconstruct the original data, ensuring efficient and reliable underwater communication. The proposed methodology is shown in Fig. 1 and Table 1 illustrates the comparison analysis of polarized and vortex communication.

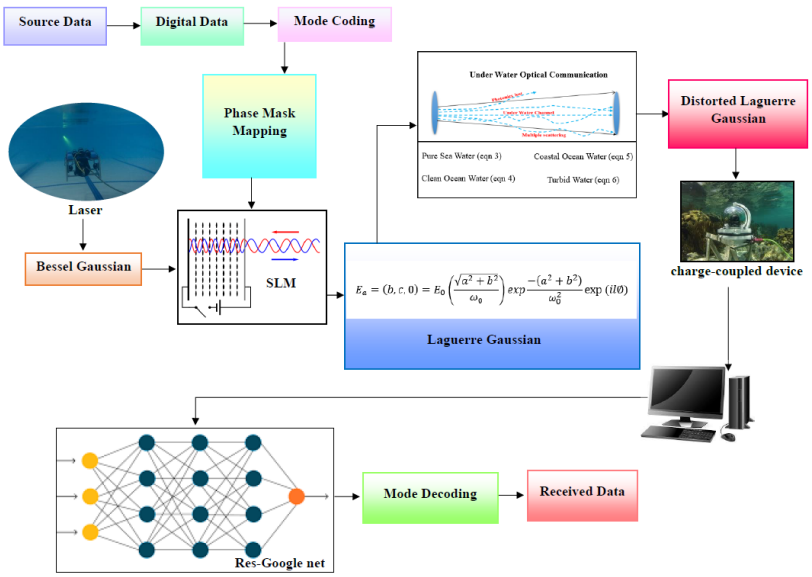

Fig. 1. Proposed methodology.

Table 1.
Comparison analysis of polarized and vortex communication.

S/No	Aspect	Polarized communication	Vortex communication
1	Beam type	Gaussian beam with linear/circular/elliptical polarization	LG beam carrying QAM
2	Information encoding	Based on polarization states	Based on OAM topological charges
3	Multiplexing capability	Limited	High
4	Turbulence sensitivity	High	Low
5	Self-healing property	No	Yes
6	Detection complexity	Simple	Moderate to high
7	Implementation cost	Low	Moderate to high
8	Suitability for underwater use	Moderate	Excellent

3.1. Bessel Gaussian

Bessel-Gaussian beam combines the characteristics of a Bessel beam (non-diffracting and self-healing) with the localized intensity of a Gaussian profile. It is generated by modulating a Gaussian beam with a Bessel function, typically using optical elements such as axicons or spatial phase masks. In the diagram, a laser source creates the Bessel-Gaussian beam, which is highly resilient to scattering and diffraction, making it ideal for long-distance optical communication, particularly underwater. Its non-diffracting property ensures that the beam maintains its spatial structure over extended ranges, even in challenging underwater environments with turbulence and particulate matter. Additionally, the self-healing capability of Bessel-Gaussian beams allows them to reconstruct their structure after encountering obstacles, making them suitable for use in environments with impurities or physical disruptions in the transmission medium.

3.2. Laguerre Gaussian (LG)

The LG beam is an optical beam characterised by a unique doughnut-shaped intensity profile and a helical phase structure, described mathematically by Laguerre polynomials. This beam is generated after the Bessel-Gaussian beam undergoes phase mask mapping through an SLM, as shown in the diagram (Fig. 1). The LG beam is widely used in MDM systems for encoding information into multiple optical modes, leveraging its OAM states for high-capacity data transmission. In underwater optical communication, the LG beam is transmitted through various types of water, including pure seawater, coastal ocean water, and turbid water, as illustrated in the diagram (Fig. 1). These water types introduce distortion due to scattering, absorption, and turbulence resulting in a distorted LG beam. To address this distortion, a charge-coupled device (CCD) captures the received optical signal, which is then further processed using a machine learning model, such as Res-GoogleNet, to decode the mode-encoded information accurately. This ensures that the transmitted data can be retrieved even in adverse underwater conditions, highlighting the robust application of LG beams in optical communication.

3.3. Mathematical formation for turbulence

The mathematical model of beam distortions during inter-ction with the medium aims to rigorously characterise and quantify the effects of underwater turbulence, scattering, and absorption on optical signal propagation. A well-defined model enables accurate prediction of beam evolution as it traverses through varying refractive index fluctuations caused by temperature and salinity gradients. Additionally, it forms a critical foundation for analysing system performance metrics such as scintillation index, BER, and SNR. By establishing a quantitative relationship between environmental parameters and beam distortion effects, such models support the optimization of beam design, modulation techniques, and decoding algorithms, thereby enhancing the robustness and efficiency of underwater optical communication systems. For example, the scintillation index σ_{SI}^2, which measures the normalized variance in received signal intensity due to turbulence, can be expressed as:

$$\sigma_{SI}^2 = \frac{\langle Is^2\rangle - \langle Is^2\rangle}{\langle Is\rangle^2}, \quad (1)$$

where Is is the received optical intensity and $<Is^2>$ denotes the ensemble average over turbulence realizations. In the context of weak turbulence, using Rytov theory, this index for a spherical wave propagating through a medium with random refractive index fluctuations is approximated as:

$$\sigma_{SI}^2 \approx 1.23 C_m^2 Ow^{\frac{7}{6}} Pd^{\frac{11}{6}}, \quad (2)$$

where C_m^2 is the refractive index structure parameter (depends on temperature and salinity gradients in water), Ow is the optical wave, Pd is the propagation distance. This model helps predict the severity of intensity fluctuations at the receiver and is instrumental in system-level design and performance analysis under underwater conditions.

Table 2.
Typical attenuation coefficients for various water types.

Water Types	$x(n^{-1})$	$y(n^{-1})$	$z(n^{-1})$
Pure sea	0.0415	0.0026	0.044
Clear ocean	0.115	0.038	0.152
Coastal	0.180	0.220	0.399
Turbid harbour	0.367	1.825	2.191

Table 2 provides an overview of typical attenuation coefficients for various kinds of water. These factors fluctuate depending on the kind of water and are linked to the proportion of dissolved particles, planktonic materials, and detritus. The following traits apply to the four main categories of water:

Pure sea water: the absorption effect is the primary limiting element. Due to the low scattering coefficient, light propagation follows a virtually straight path.

$$\text{Pure sea water} = H_2O + NaCl + \text{other salts and minerals.} \quad (3)$$

Clear ocean water: the concentration of dissolved particles is greater than in pure seawater, resulting in a growing scattering effect.

$$\text{Clean ocean water} = H_2O + NaCl + MgSO_4 + CaCO_4 + KCl. \quad (4)$$

Coastal water: the concentration of suspended particles and debris increases significantly, affecting both absorption and scattering.

$$\text{Coastal ocean water} = \rho_0(1 - \alpha(T - T_0) + \beta(S - S_0)). \quad (5)$$

Turbid harbour water: the concentration of planktonic matter, dissolved particles, and mineral components is the greatest among the four water types, resulting in significant light scattering and attenuation effects.

$$\text{Turbid water} = CC \cdot \frac{IL_{sl}}{IL_0}. \quad (6)$$

where CC is the calibration constant.

3.4. *Res-GoogleNet mode recognition*

Res-GoogleNet is used for accurate classification and decoding of received optical modes, mitigating underwater turbulence effects. Res-GoogleNet is employed to accurately recognize and decode the distorted OAM patterns. The initialization components of a CNN design were first proposed by the model. A module for inception has the following operations: 3 × 3 max pooling, 5 × 5 convolutions, 1×1 convolutions, and 3 × 3 convolutions. The reduction of the data input size for the next layer is the primary goal of pooling. This architectural layer does not have a learning process. The primary purpose of this layer is to lower computing complexity. Two popular techniques are Average Pooling and Maximum Pooling. The filters in the pooling layer are selected using N × N dimensions. The output volume has fewer channels when using a 1 × 1 convolution. Thus, with fewer layers and fewer parameters, the design was computationally superior to the other deep CNN models. The model was created to classify natural images in the ImageNet dataset domain (D1). An entirely densely linked layer sits in parallel to two convolutional layers in the dense-inception structure, an adaptation of the inception architecture. While the fully dense connection guarantees the completeness of the feature information, its depth is increased to lower the quantity of parameters. The architecture of Res-GoogleNet is shown in Fig. 2. Convolutions using different sizes of filters (1 × 1, 3 × 3, 5 × 5) can be executed in parallel by the module called inception, which enables the network to capture characteristics at various scales. A single method to depict an inception module is as follows:

$$\text{Inception}(y) = [\text{Conv}_{1\times1}(y), \text{Conv}_{3\times3}(y), \text{Conv}_{5\times5}(y), \text{MaxPool}_{3\times3}(y)]. \quad (7)$$

This notation indicates that a pooling layer and several convolutional layers are applied simultaneously to the input y. Then, along the channel dimension, the outputs are concatenated. Using the inception module as the residual function $\mathcal{F}$ in a residual block is the fundamental principle of Res-GoogleNet. The formulation of a ResNet-Inception block is as follows:

$$\mathcal{X} = \mathcal{F}_{\text{Inception}}(y, \{\mathcal{V}_j\}) + y. \quad (8)$$

Here $\mathcal{F}_{\text{Inception}}(y, \{\mathcal{V}_j\}) + y$ is the residual function generated by an inception module. The residual connection adds y straight to the inception module output, where y is the block input. The suggested architecture uses nine convolutional 2D filter widths of 128 × 64 × 32 for the flattened level and dense layers. For 224 × 224 illustrations, there is an overall of 194 × 903 × 073 training data. The n^{th} RegNet function is described in some of the following formats:

$$\mathcal{Z}_2^n = \mathbb{ReLU}\left(\mathcal{Bn}(\mathcal{W}_{12}^n * \mathcal{Z}_1^n + \mathcal{b}_{12}^n)\right) \quad (9)$$

$$[\mathcal{O}^n, \mathcal{C}^n] = \mathbb{ReLU}\left(\mathcal{Bn}\left(\mathcal{conLSTM}(\mathrm{X}_2^t, [\mathcal{O}^{n-1}, \mathcal{C}^{n-1}])\right)\right), \quad (10)$$

$$\mathcal{Z}_3^n = \mathbb{ReLU}\left(\mathcal{Bn}(\mathcal{W}_{23}^n * \mathcal{concat}[\mathcal{Z}_2^n, \mathcal{O}^n])\right), \quad (11)$$

$$\mathcal{Z}_4^n = \mathcal{Bn}(\mathcal{W}_{34}^n * \mathcal{Z}_4^n + \mathcal{b}_{34}^n), \quad (12)$$

$$\mathcal{Z}_1^{n+1} = \mathbb{ReLU}(\mathcal{Z}_1^n + \mathcal{Z}_5^n). \quad (13)$$

Where $\mathcal{b}_{12}^n$ stands for the correlation distance, 3 × 3 convolution particles $\mathcal{W}_{12}^n$, $\mathcal{W}_{23}^n$ and $\mathcal{W}_{34}^n$ consist of 1 × 1 kernels. The batch normalization stage is represented by $\mathcal{Bn}(.)$. $\mathcal{concat}(.)$ is the shorthand for the concatenation operation. The enter entity $\mathcal{Z}_2^n$ and the previous output of ConvLSTM $\mathcal{O}^n$ in (11) are the input of $\mathcal{conLSTM}$ inside the module. The $\mathcal{conLSTM}$ determines whether the data inside the memory cell is given to the $\mathcal{O}^n$ output hidden characteristic map based on the inputs source.

4. Result and discussion

In this section, the efficacy of the proposed approach is assessed using Matlab-2019b, the underwater optical communication system is discovered on a Windows OS using 16 GB of RAM and an Intel Core i7 CPU. The proposed model, compared to existing techniques such as DDNN, MCNN, and DCNN-RF, improves accuracy, evaluation metrics of accuracy, precision, recall, SNR and BER. The source parameter and description are shown in Table 3.

Table 3.
Source parameter and description.

S/No.	Source parameters	Description
1	Beam type	Bessel Gaussian (converted to LG)
2	Beam divergence angle	15°
3	Mode encoding scheme	Phase-mode encoding using OAM

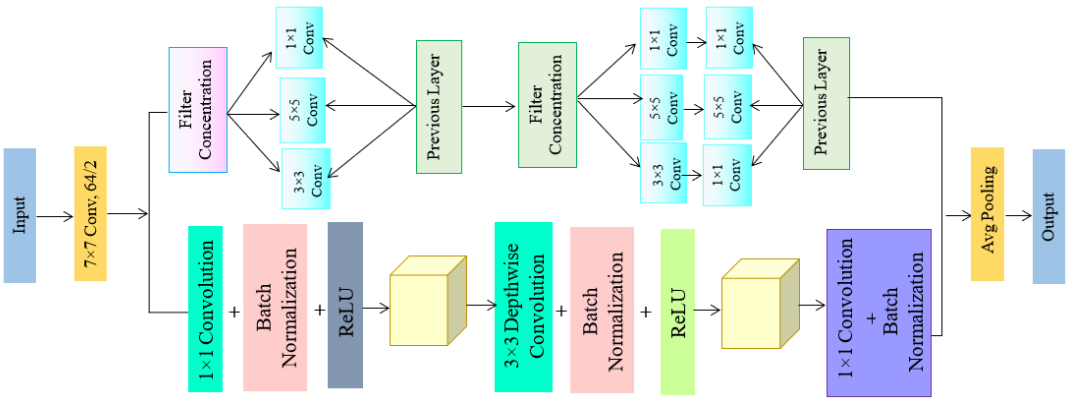

Fig. 2. Architecture of Res-GoogleNet.

The technical parameters and descriptions are presented in Table 4. Figure 3 illustrates the decomposition of three environmental signals – dissolved oxygen, water temperature, and salinity – using empirical mode decomposition (EMD). The first row displays the original signals, showing their periodic nature. The subsequent rows show their intrinsic mode functions (IMFs), which capture different frequency components. IMF1 (second row) retains the highest frequency variations, IMF2 (third row) extracts mid-frequency oscillations, and IMF3 (fourth row) captures low-frequency components and residual noise. This decomposition helps analyse underlying patterns and fluctuations in environmental parameters critical to aquatic ecosystems.

Table 4.
Technical parameter and description.

Technical parameters	Description
Spatial light modulator (SLM)	Converts Bessel to LG beam
Camera type	Underwater CCD camera
Computer CPU	Intel Core i7
RAM	16 GB
Operating system	Windows OS
Software used	Matlab-2019b

Figure 4 depicts the channel impulse response (CIR) for four distinct water types at various system configurations (FOV). The smoothness of the curve is determined by the temporal resolution Tr and the total number of simulated photons Tr. The setup contains a receiver (Rx) with a 50 cm aperture and a transmitter (Tx) with a 15° divergence angle. At 100 m, the intensity rapidly drops from its peak, with minimal trailing patterns, as photons are directed directly to the receiver. However, when water turbidity increases, the delay spread becomes more noticeable, with a 9 m connection in harbour water having poorer channel quality than the 29 m coastal link or a 50 m clear ocean link.

Figure 5 shows how the backscattering function (BSF) in dB fluctuates with link length (ζ_{rec}) for various water types, including pure, clear ocean, coastal, and turbid water. As the link length increases, BSF decreases due to signal attenuation, with clear water exhibiting the least attenuation and muddy water exhibiting the greatest. Pure water is the best medium for signal transmission, followed by clear ocean water and coastal water. However, muddy water loses signal quickly due to increased scattering and absorption caused by particulates. This trend emphasizes the critical role of water quality in underwater signal transmission.

Figure 6 illustrates four subplots that analyse the effects of nonlinear distortion on a signal in both time and frequency domains. The top-left plot represents the original signal in the time domain, displaying a clean sinusoidal waveform, which indicates that the signal is undistorted. In contrast, the top-right plot shows the signal after nonlinear distortion, where the waveform has visibly changed in amplitude and shape due to the introduction of harmonics. The bottom-left plot illustrates the frequency spectrum of the undistorted signal, which contains a single dominant frequency component, representing a pure tone. However, after nonlinear distortion, the bottom-right plot reveals multiple frequency components (harmonics), which are integer multiples of the fundamental frequency. These harmonics, a common consequence of nonlinear effects, degrade the signal quality by introducing unwanted frequency components. This analysis is crucial in fields such as RF communication, audio processing, and electronic circuit design, where maintaining signal integrity is essential.

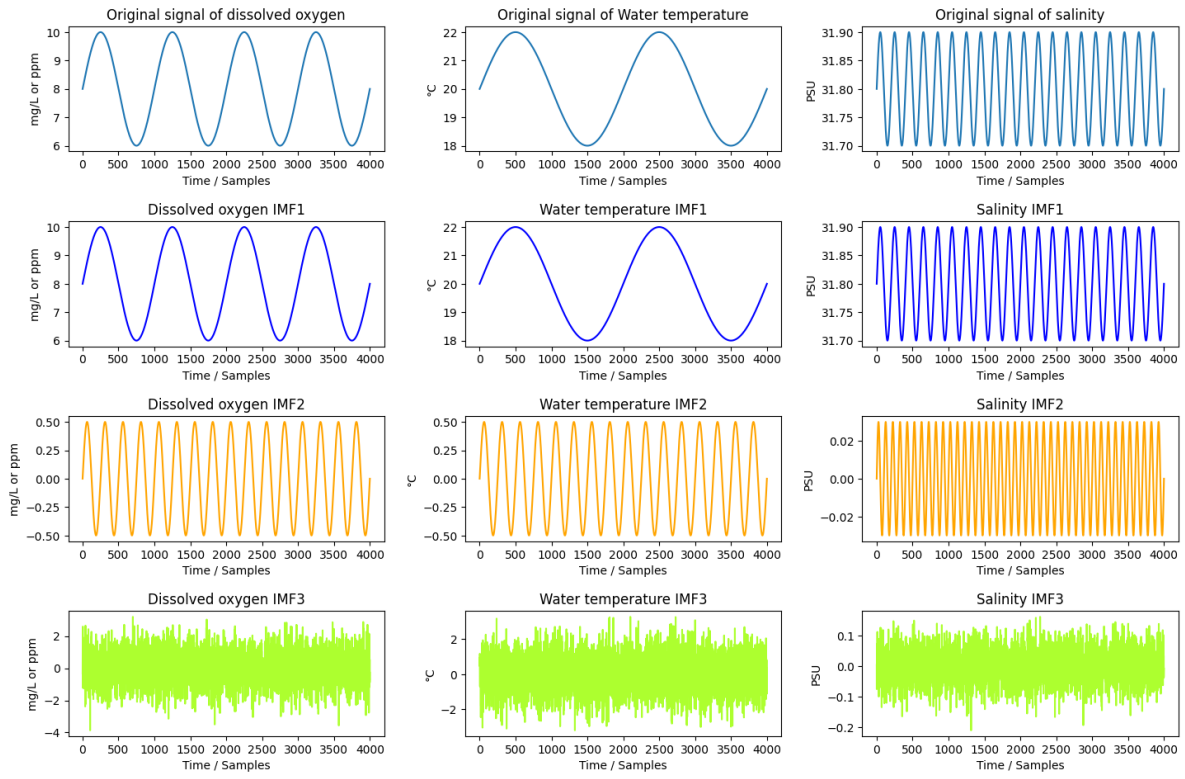

Fig. 3. Variational mode decomposition.

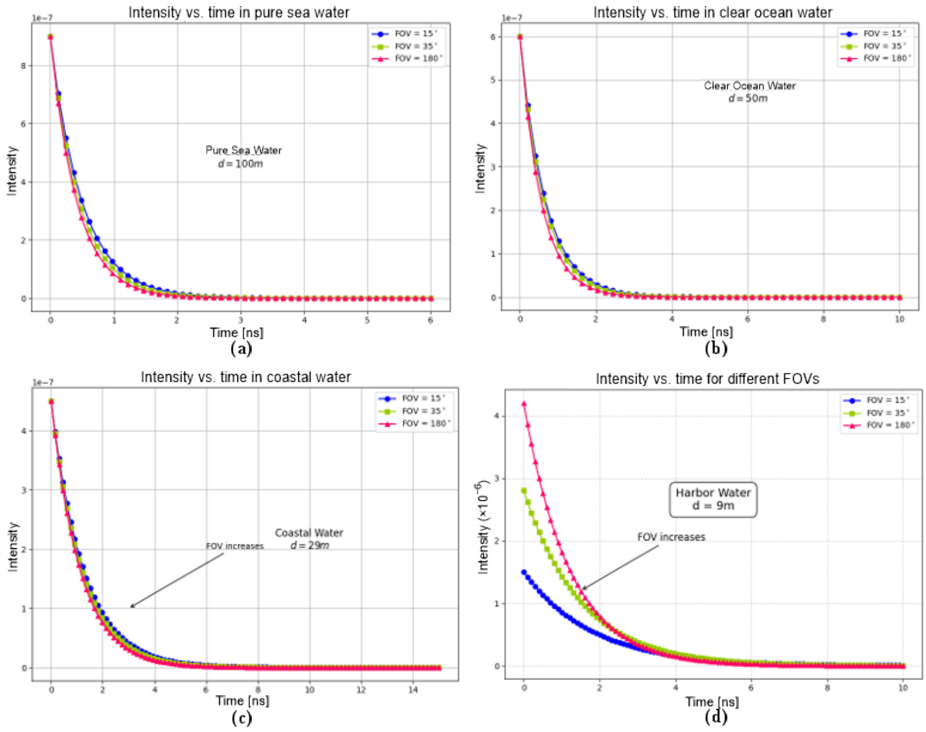

Fig. 4. Different water types under water system configurations.

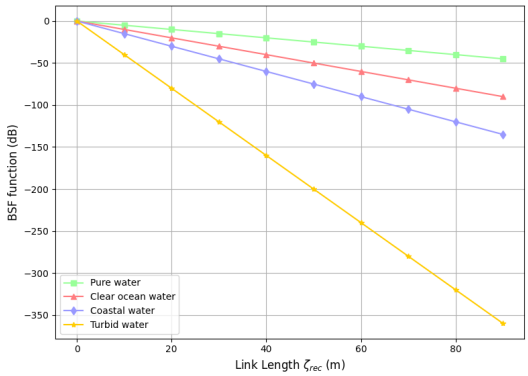

Fig. 5. Performance analysis of the BSF function.

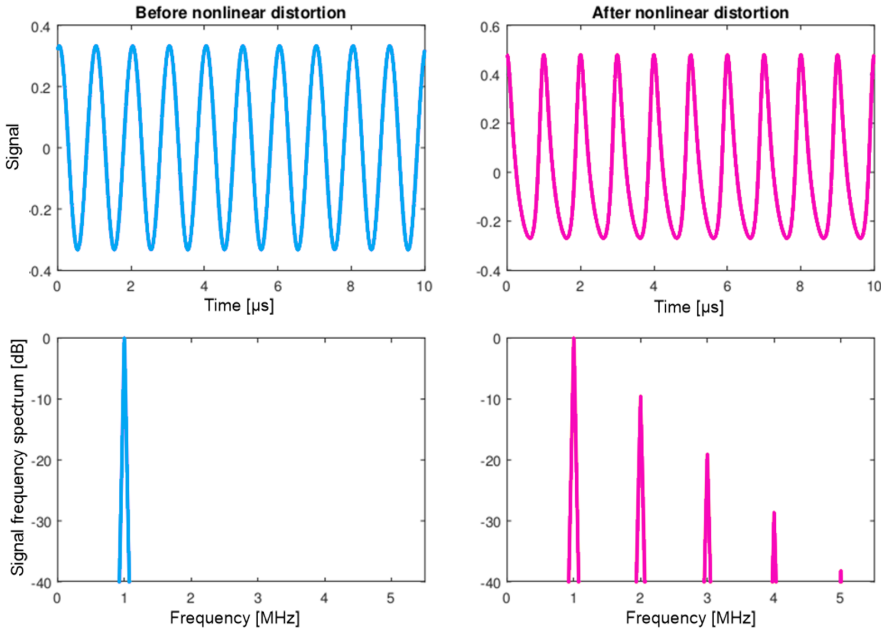

Fig. 6. Impact of nonlinear distortion on signal waveform and frequency spectrum.

Figure 7 illustrates the absorption and scattering properties of pure seawater as a function of wavelength (nm). The blue solid line indicates absorption, while the green dotted line represents scattering. Absorption is highest at shorter (UV) and longer (red) wavelengths, with a minimum in the visible light range (around 400–500 nm), which explains why seawater appears blue. Scattering remains relatively low and stable across the spectrum. The data highlights the optical characteristics of seawater, which are critical in underwater imaging, optical communication, and marine ecosystem studies.

Figure 8 illustrates the probability density functions (PDFs) of variation of hue (VOH) for the distorted and undistorted images, respectively. As can be seen, the VOH of the raw images, which are the distorted images, has a small variation range and is concentrated in small values. In contrast, the VOH of the reference images, which are the undistorted images, can vary widely with a very small probability of being small. The decision boundary for determining whether a picture is distorted is the value of the VOH at the intersection of the two graphs. Figure 8 shows that the decision boundary value is VOH = 0.0136.

Figure 9 shows the discrete-time Laguerre functions for different orders ($n = 1, 2, 3, 4, 5n = 1, 2, 3, 4, 5$) with a parameter $a = 0.8a = 0.8$. The x-axis illustrates the sample instant, while the y-axis shows the amplitude of the functions. The black solid line represents $n = 1n = 1$, the green dashed line with '×' markers illustrates $n = 2n = 2$, the brown dash-dot line depicts $n = 3n = 3$, the blue dashed line depicts $n = 4n = 4$, and the red solid line with circular markers presents $n = 5n = 5$. These functions are used in signal processing and control models for orthogonal basis representations, with higher-order functions showing more oscillatory behaviour and faster decay over time.

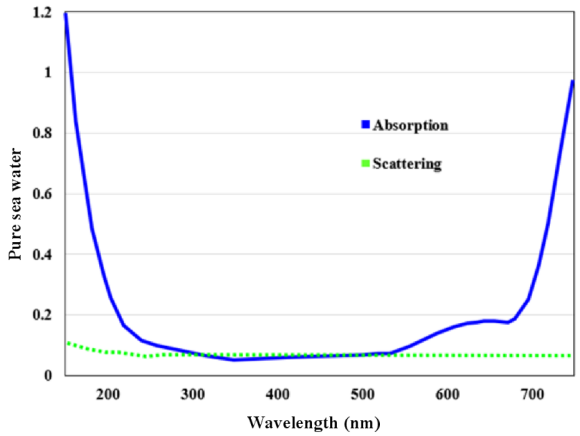

Fig. 7. Absorption and scattering properties of pure seawater.

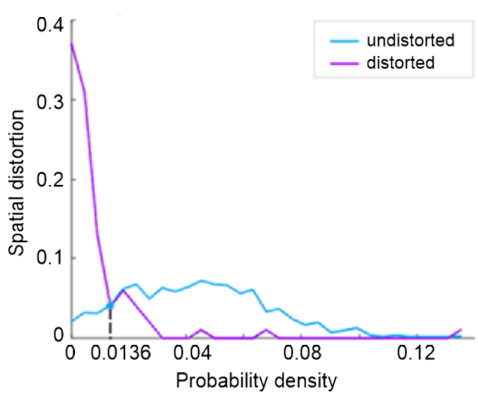

Fig. 8. Probability density function of VOH.

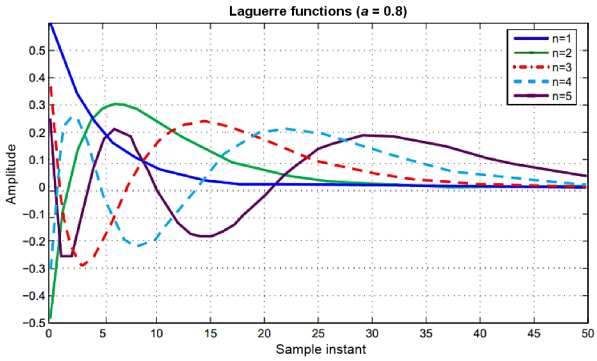

Fig. 9. Coefficients of five Laguerre polynomials with $a = 0.8$.

Figures 10 and 11 display the accuracy and loss graphs of the proposed model. Specificity, accuracy, F1 score, recall, and precision are used to evaluate the effectiveness of the suggested approach. The accuracy curve is shown in Fig. 10, where accuracy and epochs are positioned on the opposite axes. The accuracy of the model grows as the number of epochs rises. The epoch *vs*. loss curve, which illustrates how the model loss decreases with an increase in epochs, is shown in Fig. 11. The suggested model achieves an accuracy of 99.07%.

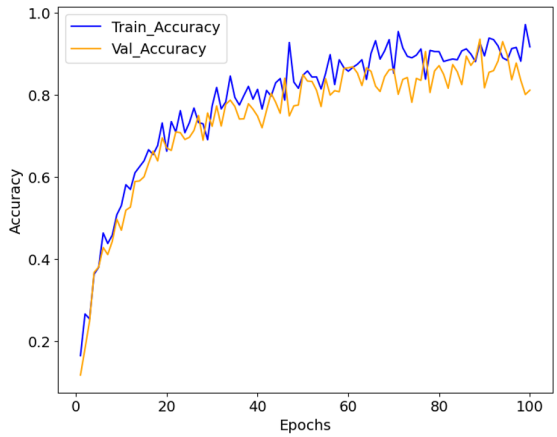

Fig. 10. Accuracy graph of the proposed model.

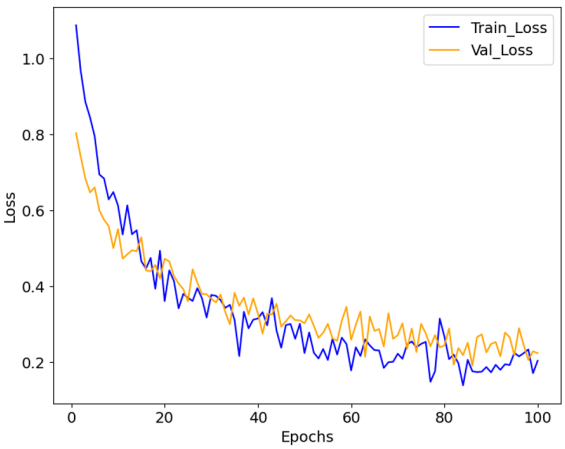

Fig. 11. Loss graph of the proposed model.

Figure 12 depicts the BER performance of different models as a function of SNR in dB. The BER is plotted on a logarithmic scale against increasing SNR values. The proposed model exhibits the best performance, achieving the lowest BER across all SNR values, particularly at higher SNRs, where the BER decreases significantly. The DCNN-RF model exhibits the worst performance, maintaining a high BER across all SNRs. The MCNN and DDNN models exhibit similar trends, with the DDNN model slightly outperforming the MCNN at higher SNRs. Numerically, the proposed model starts with a BER near 1 at 0 dB but decreases exponentially, reaching below 10^{-2} at 25 dB. MCNN and DDNN start similarly but converge to a BER slightly higher than the proposed model. DCNN-RF remains significantly higher, showing limited improvement with increasing SNR.

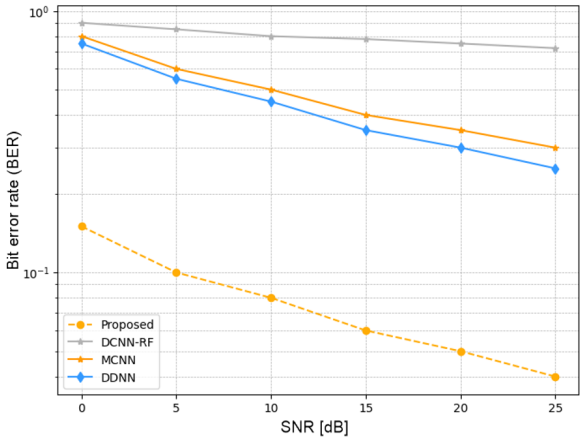

Fig. 12. Performance of BER.

Figure 13 illustrates the classification performance of four models DCNN-RF, MCNN, DDNN, and the proposed model across four categories: ocean circulation, climate change, turbulence, and weather patterns. Overall, the proposed model outperforms the others in all categories achieving near-perfect accuracy, especially excelling in weather patterns with the highest score. DDNN follows closely, particularly strong in ocean circulation and climate change. While MCNN and DCNN-RF also perform well, their accuracies are comparatively lower, especially in turbulence and weather patterns, indicating the proposed model superior generalization and effectiveness across diverse environmental conditions.

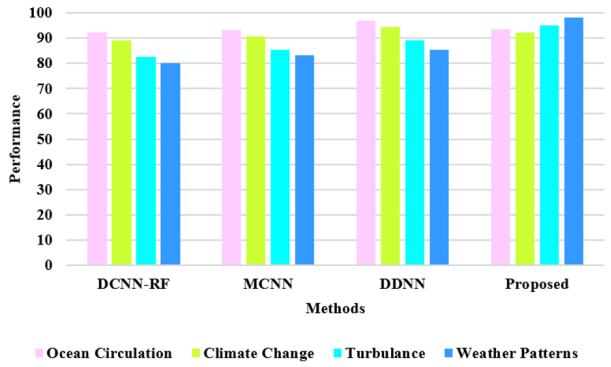

Fig. 13. Performance comparison of environmental conditions.

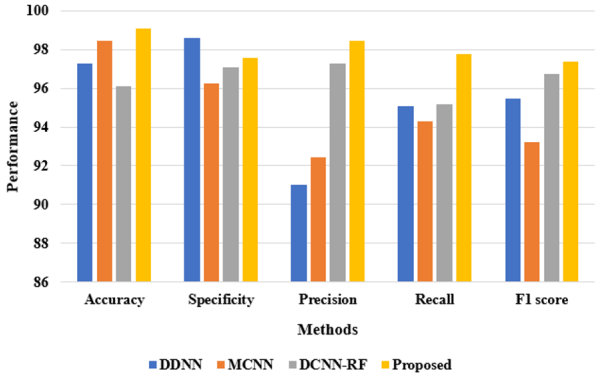

Fig. 14. Performance analysis of the proposed and existing techniques.

Figure 14 illustrates the proposed model, which outperforms existing techniques such as DDNN, MCNN, DCNN-RF, and the proposed one. The proposed model achieves a high accuracy range of 99.07%. The proposed approach achieves an accuracy rate that is more efficient than that of existing approaches. The proposed method improves its accuracy by 5.47%, 1.80%, 0.62%, and 2.97% better than DDNN, MCNN, and DCNN-RF, respectively. Figure 9 shows a graphic representation of the proposed comparative evaluation.

5. Conclusions

In this paper, a novel source data encoding and beam generation method for underwater optical communication using LG modes is proposed. Initially, the source data is converted into digital code, followed by mode matching to encode the data into specific phase modes. A Bessel-Gaussian laser beam is generated to carry the encoded information, which is then transformed into LG beams using SLM. These beams, characterised by their OAM properties, propagate through various underwater environments, including pure, clear ocean, coastal seawater and turbid water, which introduce different levels of distortion. The distorted LG beams are captured by an underwater camera and processed by a computer. A deep learning model, Res-GoogleNet, is employed to accurately recognize the mode and decode the distorted OAM patterns. Finally, the decoded mode information is used to reconstruct the original data, ensuring efficient and reliable underwater communication. The efficacy of the proposed model is assessed using Matlab-2019b, the underwater optical communication system is discovered on a Windows OS using 16 GB of RAM and an Intel Core i7 CPU. The proposed model, compared to existing techniques such as DDNN, MCNN, and DCNN-RF, improves accuracy, evaluation metrics of accuracy, precision, recall, SNR and BER. The proposed model achieves a high accuracy range of 99.07%. The proposed approach achieves an accuracy rate that is more efficient than that of existing approaches. The proposed model improves its accuracy by 5.47%, 1.80%, 0.62%, and 2.97% compared to DDNN, MCNN, and DCNN-RF, respectively. Future studies should examine actual system capacity and focus on the deployment of underwater optical channels in realistic environments, such as deep sea deployments. Since tracking and positioning

systems have been evaluated for issues with misalignment and pointing loss, they should also be considered.

Authors' statement

Research concept and design, Aravind JM and Arul Teen YP; collection and/or assembly of data, Arul Teen YP; data analysis and interpretation, Aravind JM; writing the article, Aravind JM and Arul Teen YP; critical revision of the article, Arul Teen YP; final approval of the article, Aravind JM and Arul Teen YP.

Acknowledgements

The authors would like to express their heartfelt gratitude to the supervisor for his guidance and unwavering support throughout this research.

References

[1] Selvakumar, S., Ahilan, A., Ben Sujitha, B. & Muthukumaran, N. Crystals kyber cryptographic algorithm for efficient IoT D2d communication. *Wirel. Networks* 31, 1053–1070 (2024). https://doi.org/10.1007/s11276-024-03790-6

[2] Li, Y. & Chitnis, D. Implementation and evaluation of SiPM-based photon counting receiver for IoT applications. *IEEE Internet Things J.* **11**, 20287–20299 (2024). https://doi.org/10.1109/JIOT.2024.3373448

[3] Kadam, S., Joseph, C., Kulkarni, K. J. & Raj, A. B. Lightwave modulation in free-space optical communication A Review. *Int. J. Eng. Res. Rev.* **12**, 54–89 (2024). https://doi.org/10.5281/zenodo.13847926

[4] Anisha, M. & Adlin Beenu, V. Double secure cloud medical data using euclidean distance-based Okamoto Uchiyama homomorphic encryption. *Int. J. Syst. Design Comput*. **02**, 1–7 (2024).

[5] Mokhun, I., Galushko, Y., Viktorovskaya, Y., Karabchyivskyi, M. & Bekshaev, A. Transformations of the transverse Poynting vector distribution upon diffraction of a circularly polarized paraxial beam. *J. Opt. Soc. Am. A* **41**, 382–391 (2024). https://doi.org/10.1364/JOSAA.514186

[6] Hua, M. F., Liu, S. F., Zhou, L., Bunzli, J. C. & Wu, M. M. Phosphor-converted light-emitting diodes in the marine environment: current status and future trends. *Chem. Sci.* **16**, 2089–2104 (2025). https://doi.org/10.1039/d4sc06605g

[7] Kanthavel, R., Dhaya, R. & Ahilan, A. AI-based efficient WUGS network channel modeling and clustered cooperative communication. *ACM Trans. Sens. Netw.* **18**, 1–14 (2022). https://doi.org/10.1145/3469034

[8] Ingle, R. *et al*. SERAV Deep-MAD: deep learning-based security–reliability–availability aware multiple D2D environment. *IETE J. Res.* **71**, 523–536 (2024). https://doi.org/10.1080/03772063.2024.2415502

[9] Qu, Z. & Lai, M. A review on electromagnetic, acoustic and new emerging technologies for submarine communication. *IEEE Access* **12**, 12110–12125 (2024). https://doi.org/10.1109/ACCESS.2024.3353623

[10] Chow, C.-W. Recent advances and future perspectives in optical wireless communication, free space optical communication and sensing for 6G. *J. Light. Technol.* **42**, 3972–3980 (2024). https://doi.org/10.1109/JLT.2024.3386630

[11] Prabhu, M., Muthu Kumar, B. & Ahilan, A. Slime mould algorithm based fuzzy linear CFO estimation in wireless sensor networks. *IETE J. Res.* **70**, 3407–3417. (2024). https://doi.org/10.1080/03772063.2023.2194279

[12] Patle, N., Raj, A. B., Joseph, C. & Sharma, N. Review of fibreless optical communication technology: History, evolution, and emerging trends. *J. Opt. Commun.* **45**, 679–702 (2024). https://doi.org/10.1515/joc-2021-0190

[13] Domingos, F. P. F., Lotfi, A., Ihianle, I. K., Kaiwartya, O. & Machado, P. Underwater communication systems and their impact on aquatic life – A survey. *Electronics* **14**, 7 (2024). https://doi.org/10.3390/electronics14010007

[14] Dong, X. *et al*. Towards 250-m gigabits-per-second underwater wireless optical communication using a low-complexity ANN equalizer. *Opt. Express* **33**, 2321–2337 (2025). https://doi.org/10.1364/oe.549337

[15] Malathy, E. M. *et al*. 5G network with hexagonal SDN control for highly secure multimedia communication. *IETE J. Res.* **70**, 8492–8507 (2024). https://doi.org/10.1080/03772063.2024.2394598

[16] Wang, X., Zhang, M., Zhou, H. & Ren, X. Performance analysis and design considerations of the shallow underwater optical wireless communication system with solar noises utilizing a photon tracing-based simulation platform. *Electronics* **10**, 632 (2021). https://doi.org/10.3390/electronics10050632

[17] Zhan, H. *et al*. Diffractive deep neural network based adaptive optics scheme for vortex beam in oceanic turbulence. *Opt. Express* **30**, 23305–23317 (2022). https://doi.org/10.1364/oe.462241

[18] Li, X., Xuan, H., Huang, C. & Li, Y. Orbital angular momentum mode recognition under ocean turbulence channel by DCNN-RF model based on Adma optimization. *Results Phys.* **63**, 107875 (2024). https://doi.org/10.1016/j.rinp.2024.107875

[19] Wang, M., Zhang, D., Liang, W. & Guo, W. Deep learning-based general beam synthesis for atmospheric propagation. *Opt. Express* **32**, 29159–29173 (2024). https://doi.org/10.1364/oe.530561

[20] Bai, C., Zhang, S., Wang, X., Wen, J. & Li, C. A multichannel-based deep learning framework for ocean SAR scene classification. *Appl. Sci.* **14**, 1489 (2024). https://doi.org/10.3390/app14041489

[21] Peng, Y., Chen, B., Wang, L. & Zhao, S. Diffraction deep neural network-based classification for vector vortex beams. *Chinese Phys. B* **33**, 034205 (2024). https://doi.org/10.1088/1674-1056/ad0142

[22] Yang, C. *et al*. A robust time-frequency synchronization method for underwater acoustic OFDM communication systems. *IEEE Access* **12**, 21908–21920 (2024). https://doi.org/10.1109/access.2024.3361845

[23] Mohamed, A. G. *et al*. Chaos fractal digital image encryption transmission in underwater optical wireless communication system. *IEEE Access* **12**, 117541–117559 (2024). https://doi.org/10.1109/access.2024.3446836

[24] Xing, S., Wei, B., Yu, Y. & Gong, X. A novel embedded side information transmission scheme based on polar code for peak-to-average power ratio reduction in underwater acoustic OFDM communication system. *Sensors* **24**, 7200 (2024). https://doi.org/10.3390/s24227200

[25] Alraie, H., Alahmad, R. & Ishii, K. Double the data rate in underwater acoustic communication using OFDM based on subcarrier power modulation. *J. Mar. Sci. Technol.* **29**, 457–470 (2024). https://doi.org/10.1007/s00773-024-00989-2

[26] Mokhun, I., Galushko, Y., Viktorovskaya, Y., Karabchyivskiy, M. & Bekshaev, A. Transformations of the transverse Poynting vector distribution upon diffraction of a circularly polarized paraxial beam. *J. Opt. Soc. Am. A* **41**, 382–391 (2024)